

# Catalytic Interfaces-Enriched Hybrid Hollow Spheres Sulfur Host for Advanced Li–S Batteries

Jin-Lin Yang, Shi-Xi Zhao,\* Xiang-Tian Zeng, Yi-Ming Lu, and Guo-zhong Cao\*

Lithium–sulfur (Li–S) batteries are considered as a promising next-generation energy storage technology due to its high energy density over 2500 Wh kg<sup>-1</sup> and low cost. Its development and application require to overcome several obstacles including the large volume change, the low electrical conductivity of S/Li<sub>2</sub>S, and the shuttle effect of lithium polysulfides (LIPs). In this work, the hollow N-doped carbon spheres (NHCS) decorated with nanosized SnS<sub>2</sub> (NHCS-SnS<sub>2</sub>) are synthesized and investigated to host sulfur used as the cathode for Li–S batteries. Highly conductive NHCS offer a large specific surface area and robust confinement for active material S, while SnS<sub>2</sub> nanoparticles provide efficient chemisorption of LIPs and promote the deposition of solid Li<sub>2</sub>S. The NHCS-SnS<sub>2</sub>/S cathode materials deliver a high discharge capacity 1344 mAh g<sup>-1</sup> at 0.2 C and a low capacity decay over 200 cycles at 0.5 C. The outstanding cycling stability at 0.2 C with high sulfur loading of 3.0–3.1 mg cm<sup>-2</sup> can also be readily attained. The excellent electrochemical performance is attributed to possible triple phase catalytic effect of NHCS-SnS<sub>2</sub> and electrolyte, and such structure permits the full utilization of active materials from S<sub>8</sub> to Li<sub>2</sub>S.

(LIPs) (Li<sub>2</sub>S<sub>n</sub>, 4 ≤ n ≤ 8), and 3) large volume fluctuation originated from the conversion between S<sub>8</sub> and Li<sub>2</sub>S during cycling. Sulfur cathode materials need to be designed and synthesized to circumvent the above technical obstacles for the further development of Li–S batteries.

The sulfur host should possess the following features: acting as a physical confinement for sulfur to accommodate the volume change, providing chemical adsorption for LIPs to reduce the shuttle effect, having high electronic conductivity, and offering sufficient active sites for solid Li<sub>2</sub>S<sub>2</sub> and Li<sub>2</sub>S deposition.<sup>[3]</sup> In the past decade, carbon-based materials such as mesopores carbon,<sup>[4]</sup> carbon nanotube,<sup>[5]</sup> graphene,<sup>[6]</sup> hollow carbon spheres,<sup>[7]</sup> and carbon fibers<sup>[8]</sup> have been employed as the sulfur host material. These carbon-based materials with large pore volume can not only hold the sulfur and electrolyte but also offer the 3D electron transport network.

However, carbon-based materials cannot efficiently block the diffusion of LIPs due to their weak polarity. Although doping N, O, S, and B can induce polar sites and enhance the interaction with the Li atoms in LIPs,<sup>[9]</sup> it does not reduce the shuttling of LIPs due to the weak chemisorption.<sup>[10]</sup> To reduce and block the diffusion of LIPs, some polar materials such as metal oxides,<sup>[11]</sup> sulfides,<sup>[12]</sup> carbides,<sup>[13]</sup> and nitrides<sup>[14]</sup> have been widely investigated and introduced owing to their strong chemical interaction with LIPs species. However, their poor electronic conductivity generally leads to the interruption of LIPs reduction, and some oxides such as MoO<sub>3</sub> and V<sub>2</sub>O<sub>5</sub> having too strong adsorption to LIPs could result in the destruction of LIPs species.<sup>[15]</sup> In this case, conductive carbon matrix functionalized with appropriate polar materials is expected to realize both of their advantages.<sup>[16]</sup> Because of the indirect charge transportation in these polar mediator, LIPs species adsorbed by polar mediator tend to diffuse from the polar surface to the nearby conductive carbon matrix and then are further reduced to solid Li<sub>2</sub>S.<sup>[17]</sup> On this basis, two representative strategies are proposed to realize the above intentions. One is to construct a cooperative interfaces between N-doped carbon matrix and polar mediator to obtain dual interaction based on N–Li and M–S\* (S\*, S atoms in LIPs species) binding;<sup>[18]</sup> Another is to adopt heterostructure on conductive substrate like TiO<sub>2</sub>-TiN,<sup>[19]</sup> VO<sub>2</sub>-VN<sup>[20]</sup> to let the long-chains LIPs captured by oxides, and allow the Li<sub>2</sub>S deposit on nitrides. In another word, these hybrid structure can


## 1. Introduction

To meet the demand for achieving high energy density and long cycle life for new generation electric vehicles and portable devices, Li–sulfur batteries are promising due to its ultrahigh energy density (2500 Wh kg<sup>-1</sup>) and the low cost of sulfur.<sup>[1]</sup> The development of Li–S batteries is, however, impeded by the following technical challenges:<sup>[2]</sup> 1) intrinsic electronic insulating nature of sulfur (5 × 10<sup>-30</sup> S cm<sup>-1</sup>) and final products Li<sub>2</sub>S<sub>2</sub>/Li<sub>2</sub>S, 2) shuttle effect of intermediate lithium polysulfides

J.-L. Yang, Prof. S.-X. Zhao, X.-T. Zeng, Y.-M. Lu  
Shenzhen International Graduate School  
Tsinghua University  
Shenzhen 518055, China  
E-mail: zhaosx@sz.tsinghua.edu.cn

J.-L. Yang, X.-T. Zeng, Y.-M. Lu  
School of Materials Science and Engineering  
Tsinghua University  
Beijing 100084, China

Prof. G.-z. Cao  
Department of Materials Science and Engineering  
University of Washington  
Seattle, WA 98195, USA  
E-mail: gzcao@uw.edu

 The ORCID identification number(s) for the author(s) of this article can be found under <https://doi.org/10.1002/admi.201901420>.

DOI: 10.1002/admi.201901420

limit the original solid–liquid–solid conversion of active materials occurred on the interfaces in order to promote the reaction kinetics. Based on above research results, an ideal sulfur host should possess the moderate adsorption to LIPSSs, fast LIPSSs diffusion rate on polar surface and adequate  $\text{Li}_2\text{S}$  nucleation sites simultaneously.

Recently, metal sulfides such as  $\text{Co}_9\text{S}_8$ ,<sup>[21]</sup>  $\text{NiS}_2$ ,<sup>[22]</sup>  $\text{FeS}_2$ ,<sup>[23]</sup>  $\text{ZnS}$ ,<sup>[24]</sup>  $\text{VS}_2$ ,<sup>[25]</sup>  $\text{SnS}_2$ ,<sup>[26]</sup>  $\text{CoS}_2$ ,<sup>[27]</sup> and  $\text{WS}_2$ <sup>[28]</sup> were widely studied to propel the LIPSSs conversion and avoid shuttling due to their higher electron conductivity compared to oxides and their easier synthesis process compared to carbides or nitrides. Based on previous calculations, the effectively chemical adsorption to LIPSSs can be achieved through Lewis-acid interaction of  $\text{Li-S}$  or  $\text{S}^*-\text{M}$  bonding.<sup>[29]</sup> However, most of these hybrid structure contained a high weight ratio or mesosized of metal sulfides, which result in the decrease of the conductivity of whole electrode. Therefore, it is significant to optimize the catalytic effect by downsizing the microsized sulfides to nanosized polar sites anchored on the carbon matrix.

In this study, N-doped carbon hollow spheres decorated with  $\text{SnS}_2$  and loaded with sulfur (NHCS- $\text{SnS}_2/\text{S}$ ) were synthesized and served as the cathodes for Li–S batteries. Such structured sulfur cathodes offer a porous 3D conductive network to facilitate electron transport and electrolyte infiltration, and N atoms in NHCS could promote the chemisorption of LIPSSs. The inner void space in NHCS could accommodate the volume expansion of the discharge products. Different from the traditional hollow sulfur hosts such as layer coating ( $\text{TiO}@C\text{-HS}$ ), yolk-shell ( $\text{YSC}@Fe_3O_4$ ) or single side modification ( $\text{NiS}@C\text{-HS}$ ),<sup>[30]</sup> the dispersed distribution of  $\text{SnS}_2$  on NHCS surface could offer abundant active sites for adsorbing LIPSSs and depositing  $\text{Li}_2\text{S}_2/\text{Li}_2\text{S}$ . The low content of  $\text{SnS}_2$  does not reduce the conductivity of NHCS. Such cathode has demonstrated excellent electrochemical performance in Li–S batteries including high capacity, cycling stability, fast kinetic conversion of LIPSSs, and controlled deposition of solid  $\text{Li}_2\text{S}$ .

## 2. Results and Discussion

### 2.1. Formation and Characterization of NHCS- $\text{SnS}_2/\text{S}$ Composite

Figure 1a illustrates the fabrication process: tetraethyl orthosilicate (TEOS) was used to form  $\text{SiO}_2$  sphere template first through hydrolysis-condensation processing.<sup>[31]</sup> Then the polymerization of resorcinol–formaldehyde oligomers took place and coated on the template, such oligomers finally turned into carbon layer after calcined in nitrogen (Figure 1b,f).<sup>[32]</sup> Sequentially,  $\text{SiO}_2$  was etched by NaOH solution and the as prepared hollow carbon spheres were doped by nitrogen atoms to obtain NHCS through a facile hydrothermal process.<sup>[33]</sup> Monodisperse NHCS with an average diameter of 400 nm are shown in scanning electron microscopy (SEM) and transmission electron microscope (TEM) images (Figure 1c and Figure S1a, Supporting Information) and the shell thickness was about 7 nm (Figure 1g).  $\text{SnO}_2$  nanoparticles were then incorporated to NHCS by slow hydrolysis of  $\text{Sn}^{2+}$  with the aid of hydrochloric acid.<sup>[34]</sup> Figure 1d and Figure S1b in the Supporting Information showed the hybrid structures with

identical diameter as initial NHCS and the nanosized  $\text{SnO}_2$  nanoparticles with uniform dispersion can also be identified. The content of  $\text{SnO}_2$  is around 23 wt% as shown in Figure S3 in the Supporting Information. Finally, NHCS- $\text{SnS}_2/\text{S}$  were formed after sulfur loading process at 300 °C. During this period, a majority of sulfur evaporated and infused into the pores carbon layer, a fraction of sulfur simultaneously reacted with and converted  $\text{SnO}_2$  nanoparticles to  $\text{SnS}_2$ . SEM and TEM images (Figure 1e–h and Figure S2a, Supporting Information) show that there is almost no bulk sulfur agglomeration and the hybrid structure maintained its original spherical morphology, indicating that the sulfur had effectively impregnated in the pores of NHCS as desired.  $\text{SnS}_2$  nanocrystals with a homogeneous distribution on the shell surface of NHCS can be clearly observed. The corresponding selected area electron diffraction (SEAD) pattern shows the polycrystalline state of dispersed  $\text{SnS}_2$  (inset of Figure 1e). In high-resolution transmission electron microscopy (HRTEM) image, the d-spacing of 0.28 and 0.32 nm along (101) and (100) direction of  $\text{SnS}_2$  can be distinguished in Figure 1i, such nanosized  $\text{SnS}_2$  was quiet similar to the sulfurization of  $\text{SnO}_2$  precursor via  $\text{H}_2\text{S} + \text{Ar}$  gas treatment or hydrothermal method as reported.<sup>[35]</sup> The corresponding energy dispersive spectrometer (EDS) mapping of Figure 1h is shown in Figure S2b in the Supporting Information. Such sulfurization method by using sulfur powder as sulfur source to react with oxide was early applied to preparing  $\text{MoS}_2$  from  $\text{MoO}_2$ .<sup>[36]</sup> We speculate that the possible mechanism of the sulfurization process could be assigned to the disproportionation of sulfur at high temperature ( $\text{S}_8 + \text{SnO}_2 \rightarrow \text{SO}_2 + \text{SnS}_2$ ).

X-ray diffraction (XRD) patterns of NHCS, NHCS- $\text{SnO}_2$ , and NHCS- $\text{SnS}_2/\text{S}$  are shown in Figure 2a. NHCS sample reveals amorphous phase and NHCS- $\text{SnO}_2$  sample exhibits the diffraction peak of  $\text{SnO}_2$  (Joint Committee on Powder Diffraction Standards (JCPDS): 77-0450) on the amorphous NHCS. After sulfur loading, the element sulfur (JCPDS: 86-1278) could be identified clearly. Besides, berndtite-2T  $\text{SnS}_2$  (JCPDS: 01-1010) with the crystallinity of hexagonal can also be detected in NHCS- $\text{SnS}_2/\text{S}$  samples, diffraction peaks at 15°, 32°, 41.9°, and 50.0° are indexed to (001), (101), (102), and (110) planes of  $\text{SnS}_2$ . After removal of sulfur using  $\text{CS}_2$  solution, the diffraction peaks of sulfur disappeared and the rest matched to hexagonal  $\text{SnS}_2$  well. XRD results further verify the incorporation of sulfur and the conversion of  $\text{SnO}_2$  to  $\text{SnS}_2$  through the sulfurization process. The sulfur loading is around 70 wt% for both NHCS/S and NHCS- $\text{SnS}_2/\text{S}$  composites (Figure S4, Supporting Information).

The element mapping of NHCS- $\text{SnS}_2/\text{S}$  collected by EDS analysis under dark field displays the uniform and spherical-like distribution of C, Sn, and S on the hybrid spheres (Figure S5, Supporting Information), which confirms the uniform distribution of  $\text{SnS}_2$  and indicates that element sulfur tends to adhere to the inner wall of NHCS rather than a big bulk wrapped by carbon shell, which is similar to the phenomenon of the multi-shell carbon spheres as reported.<sup>[37]</sup> Accordingly, the nitrogen sorption isotherms of NHCS, NHCS- $\text{SnO}_2$ , and NHCS- $\text{SnS}_2/\text{S}$  are shown in Figure S6 in the Supporting Information. For NHCS, a typical IV type isotherm with a large specific area about 580  $\text{m}^2 \text{g}^{-1}$ , high total pore volume about 2.76  $\text{cm}^3 \text{g}^{-1}$ , and an average pore size of 2 nm reflects a promising porous substrate framework for sulfur loading and electrolyte permeating. After



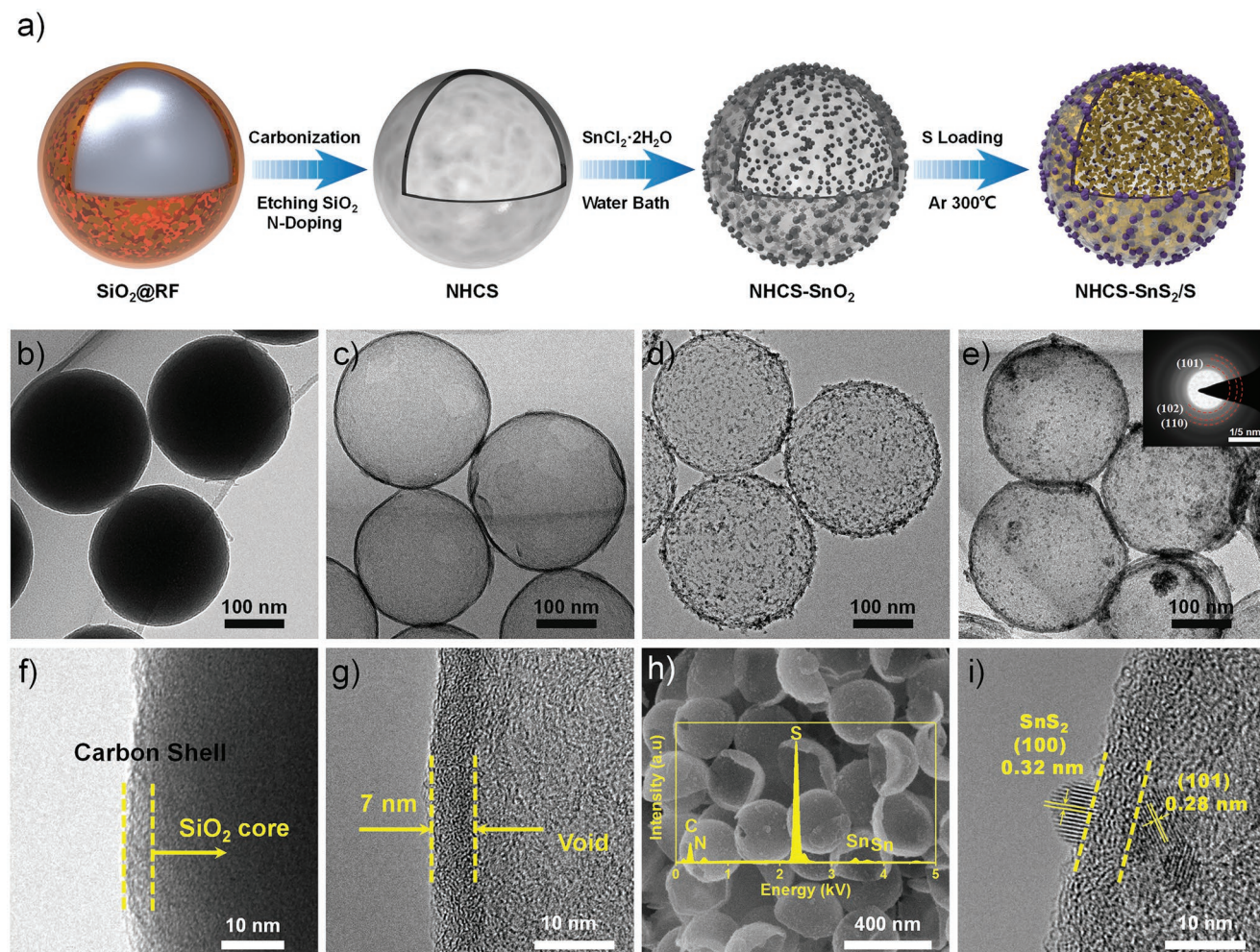


**Figure 1.** a) Schematic illustration of the synthesis process of NHCS-SnS<sub>2</sub>/S hybrid structure. TEM images of b) SiO<sub>2</sub>@C core-shell structure, c) NHCS, d) NHCS-SnO<sub>2</sub> precursor, e) NHCS-SnS<sub>2</sub>/S, and the corresponding SEAD pattern was shown inset. High-magnification TEM images of f) SiO<sub>2</sub>@C and g) NHCS. h) SEM image of NHCS-SnS<sub>2</sub>/S and the inset was EDS spectrum. i) HRTEM image of NHCS-SnS<sub>2</sub>/S.

decorated by SnO<sub>2</sub> precursor, the specific surface area and total pore volume drop to 440.7 m<sup>2</sup> g<sup>-1</sup> and 1.63 cm<sup>3</sup> g<sup>-1</sup> because of the blocking of some pores. Meanwhile, the surface area, total pore volume and the maximum peak of the pore size revealed a sharp shrinkage after sulfur infusion (22.6 m<sup>2</sup> g<sup>-1</sup>, 0.19 cm<sup>3</sup> g<sup>-1</sup>), which demonstrates that the sulfur has infused into the pores of the carbon shell. The Brunauer, Emmett and Teller results are listed in Table S1 in the Supporting Information.

The NHCS-SnS<sub>2</sub>/S composite was further characterized by X-ray photoelectron spectroscopy (XPS). The survey spectrum presents the coexistence of element Sn, S, N, and C (Figure S7, Supporting Information) in NHCS-SnS<sub>2</sub>/S sample. Compared the binding energy of Sn 3d before and after sulfur loading in Figure 2b, a negative shift about 0.3 eV from 487.4 to 487.1 eV (Sn<sup>4+</sup> 3d<sub>5/2</sub>) and 495.7 to 495.4 eV (Sn<sup>4+</sup> 3d<sub>3/2</sub>) is observed, suggesting the sulfurization transformation from SnO<sub>2</sub> to SnS<sub>2</sub>.<sup>[38]</sup> Two weak peaks situated at higher binding energy marked by blue may be ascribed to the surface oxidation of SnS<sub>2</sub> or a few residual SnO<sub>2</sub>, which cannot be detected by XRD. In the S2p spectrum (Figure 2c), two peaks located at 161.99 and 163.0 eV are ascribed to the anion S<sup>2-</sup> 2p<sub>3/2</sub> and

S<sup>2-</sup> 2p<sub>5/2</sub> in SnS<sub>2</sub>, respectively.<sup>[35b]</sup> The signals of element sulfur (163.99 eV/165.13 eV) can also be found.<sup>[39]</sup> In addition, the peaks around 166.04 and 167.95 eV could be identified as the sulfate or thiosulfate for the oxidation of sulfur.<sup>[40]</sup> In Figure 2d, the N1s curve exhibits four types of N atoms on the surface of carbon spheres with a low atomic content of 3.6%. Pyridinic N, amino/imino N, pyrrolic N, and quaternary N are referred to the peaks at 398.44, 399.36, 400.95, and 403.48 eV, respectively.<sup>[33,41]</sup> The results imply that N atoms were successfully doped into the lattice of carbon. Among them, pyridinic N and pyrrolic N could serve as anchor sites to LIPSSs. In the C1s spectrum (Figure S8, Supporting Information), four board peaks at 284.75, 285.47, 287.5, and 289.1 eV are related to the bond of C=C, C-N/C-S, C=O, and O-C=O, respectively.<sup>[42]</sup> Which indicates a large amount of oxygen functional groups on NHCS surface. These functional groups could also make a contribution to restrict LIPSSs shuttling.<sup>[43]</sup> The Raman spectra of HCS and NHCS (Figure S9, Supporting Information) showed the decline of graphitization degree after N-doping, indicating that the increase of defect sites on carbon spheres with the introduction of nitrogen.<sup>[44]</sup> NHCS-SnS<sub>2</sub> showed a prominent band of

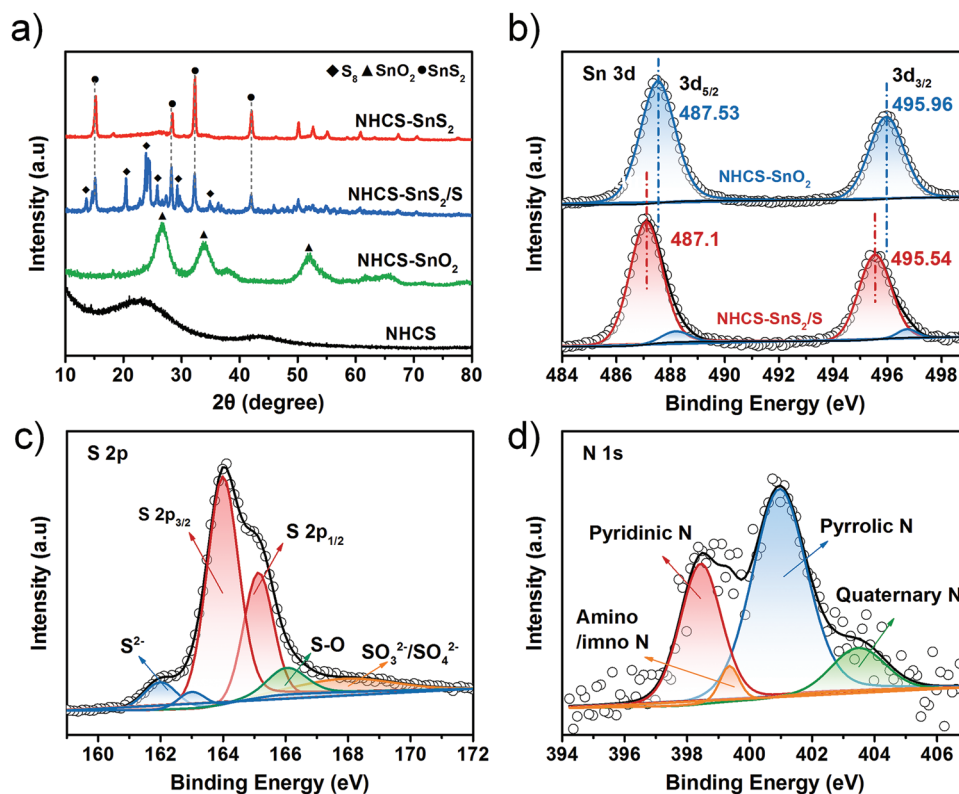


**Figure 2.** a) XRD patterns of NHCS, NHCS-SnO<sub>2</sub>, NHCS-SnS<sub>2</sub>/S, and NHCS-SnS<sub>2</sub>. XPS spectra of b) Sn 3d of NHCS-SnO<sub>2</sub> and NHCS-SnS<sub>2</sub>/S and c,d) S2p and N1s of NHCS-SnS<sub>2</sub>/S

SnS<sub>2</sub> around 310 cm<sup>-1</sup> and almost no SnO<sub>2</sub> (632 cm<sup>-1</sup>) can be found in the spectra.

## 2.2. Electrochemical Performance of NHCS-SnS<sub>2</sub>/S Composite

The cyclic voltammetry (CV) results are shown in **Figure 3a**. Both NHCS/S and NHCS-SnS<sub>2</sub>/S electrodes exhibit two cathodic peaks and one anodic peak. For NHCS-SnS<sub>2</sub>/S electrode, the anodic peak located at 2.4 V is attributed to the oxidation of Li<sub>2</sub>S<sub>2</sub>/Li<sub>2</sub>S to S<sub>8</sub>, and the two cathodic peaks around 2.27 and 2.023 V represent the conversion from S<sub>8</sub> to long chain LIPs and then to solid Li<sub>2</sub>S<sub>2</sub>/Li<sub>2</sub>S respectively.<sup>[7]</sup> Compared to the NHCS electrode, a positive shift of two cathodic peaks (the inset of **Figure 3a**) and a slight negative shift of anodic peak in NHCS-SnS<sub>2</sub>/S indicates that the SnS<sub>2</sub> modification could significantly reduce the electrochemical polarization of the cell and facilitate the reaction rate. As shown in **Figure S10** in the Supporting Information, a small difference between the 1st and 2nd CV scan of the NHCS-SnS<sub>2</sub>/S electrode can be attributed to the activation or redistribution of the sulfur.<sup>[45]</sup> In the subsequent scans, the well overlap of the CV curves demonstrates the good electrochemical reversibility of NHCS-SnS<sub>2</sub>/S electrode. **Figure 3b** displays the rate performance of NHCS/S and NHCS-SnS<sub>2</sub>/S electrode.

When cycled at 0.2, 0.5, 1, and 2 C, the discharge capacity of NHCS-SnS<sub>2</sub>/S was 1344, 921, 822, and 757 mAh g<sup>-1</sup>, respectively, much superior to the NHCS/S cathode. After cycled

at a high current density, the reversible discharge capacity of NHCS-SnS<sub>2</sub>/S composite returned to 902 mAh g<sup>-1</sup>, indicating the remarkable rate performance. The galvanostatic charge/discharge profiles of NHCS-SnS<sub>2</sub>/S at various current rates are shown in **Figure 3c**. All the profiles exhibit two discharge plateaus and one well-defined charge plateau with high coulombic efficiency even the current density increased to 2 C. To elucidate the capacity stabilities of SnS<sub>2</sub> incorporation, the long-term cycling performance of NHCS/S and NHCS-SnS<sub>2</sub>/S electrodes is shown in **Figure 3d,e**. After activated at 0.1 C, the NHCS-SnS<sub>2</sub>/S electrode shows discharge capacity around 970 mAh g<sup>-1</sup> at 0.5 C, and the capacity of can still be remained at 713 mAh g<sup>-1</sup> after 200 cycles, with the capacity decay of 0.133% per cycle, much superior to the value of NHCS/S electrode (0.192% per cycle). When cycled at 1 C, NHCS-SnS<sub>2</sub>/S also delivers higher initial discharge capacity around 901 mAh g<sup>-1</sup> than NHCS/S (789 mAh g<sup>-1</sup>). What is more, a capacity of 634 mAh g<sup>-1</sup> could be maintained after 200 cycles, higher than the value of NHCS/S electrode (433 mAh g<sup>-1</sup>). The corresponding charge–discharge curves after the 1st and the 200th cycle at 1 C were displayed in **Figure S11** in the Supporting Information. The lower gap between charge–discharge plateau potentials and longer plateaus of NHCS-SnS<sub>2</sub>/S electrode in both 1st and 200th cycle indicating the lower electrochemical polarization and higher capacity remaining compared with the NHCS/S electrode. Furthermore, NHCS-SnS<sub>2</sub>/S electrodes with higher sulfur loading (3.0–3.1 mg cm<sup>-2</sup>) were also prepared. The discharge capacity was 1278, 1216, 1010, 847,



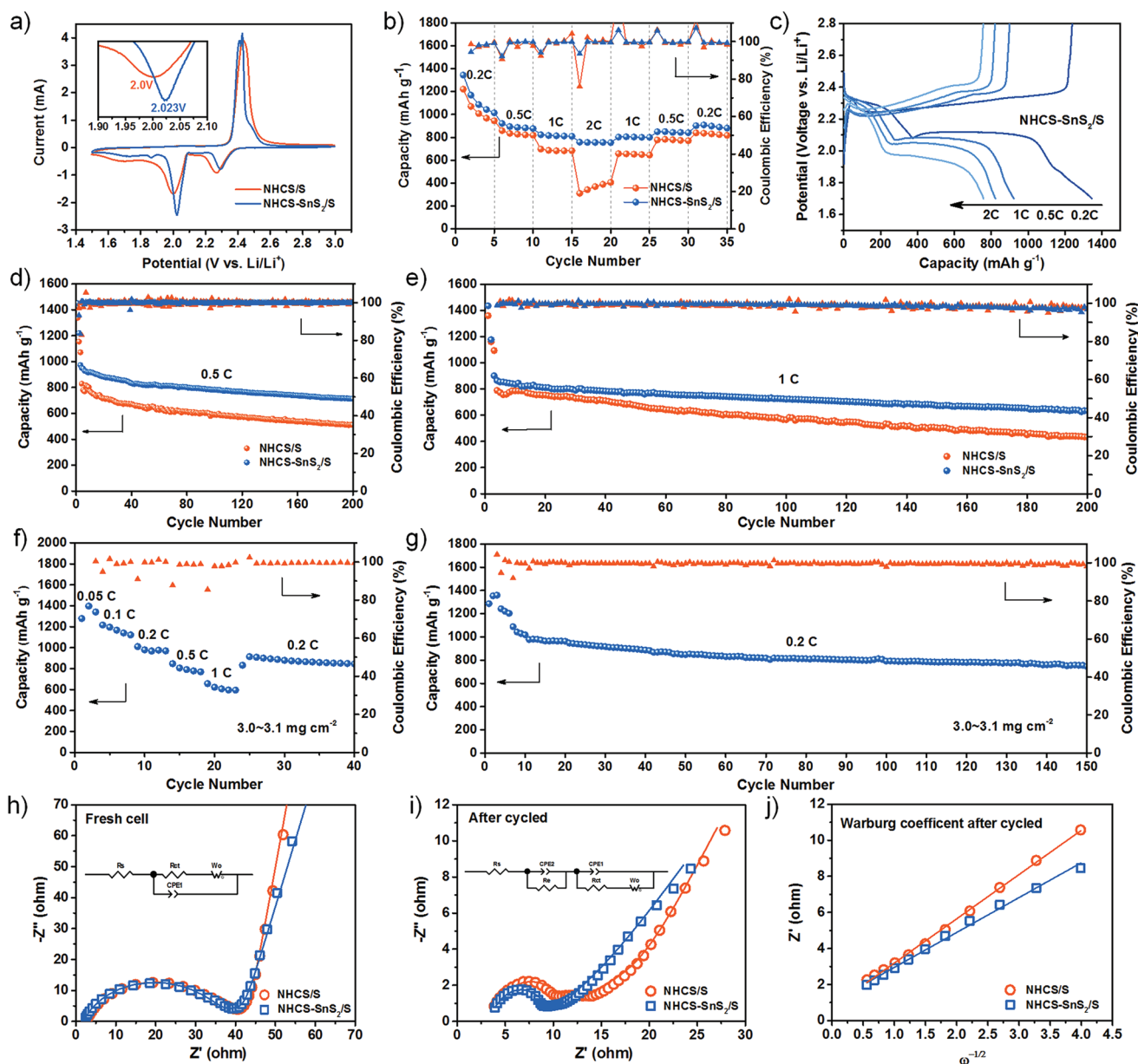


**Figure 3.** Electrochemical performance of NHCS/S and NHCS-SnS<sub>2</sub>/S electrode. a) CV curves, b) rate performance from 0.2 to 2 C, c) charge/discharge voltage profiles of NHCS-SnS<sub>2</sub>/S electrode at different current density, d) cycling performance at 0.5 C over 200 cycles, e) cycling performance at 1 C over 200 cycles, f, g) rate performance and long term cycle of NHCS-SnS<sub>2</sub>/S electrodes with sulfur loading around 3.0–3.1 mg cm<sup>-2</sup>, h, i) Nyquist impedance plots and the corresponding fitting curves of NHCS/S and NHCS-SnS<sub>2</sub>/S electrodes before and after cycled, and j) Warburg coefficient of NHCS/S and NHCS-SnS<sub>2</sub>/S electrodes after cycled at 0.5 C.

and 657 mAh g<sup>-1</sup> under 0.05, 0.1, 0.2, 0.5, and 1 C respectively (Figure 3f and Figure S12, Supporting Information). Figure 3g displays the long-term cycling of high sulfur loading electrode, the initial reversible discharge capacity of NHCS-SnS<sub>2</sub> at 0.2 C was 1094 mAh g<sup>-1</sup>, which still maintained around 750 mAh g<sup>-1</sup> after 150 cycles with the high coulombic efficiency (99.4%), representing a small decay rate and high capacity retention even the electrode was thickly coated. We also tested NHCS-SnS<sub>2</sub> electrode in the voltage window of 1.7–2.8 V (Figure S13, Supporting Information). It is worth mentioning that the capacity contributed by NHCS-SnS<sub>2</sub> can be ignored. The remarkable

capacity stability of NHCS-SnS<sub>2</sub>/S reveals that the polarity SnS<sub>2</sub> modification can efficiently fix LIPSS, thus prevent the LIPSS shuttling and self-discharging and bring about higher capacity retention. The electrochemical performance of NHCS-SnS<sub>2</sub>/S compared to some hybrid or hollow sulfur hosts reported in recent years are listed in Table S3 in the Supporting Information.

Electrochemical impedance spectroscopy (EIS) analysis of NHCS-SnS<sub>2</sub>/S and NHCS/S electrode was measured to clarify the improvement of electrochemical performance of the SnS<sub>2</sub> modification. All data were analyzed by fitting the Nyquist plots

with the equivalent (inset of Figure 3h,i) circuits and listed in Table S2 in the Supporting Information. As shown in Figure 3h, the contact resistance ( $R_c$ ) and charge-transfer resistance ( $R_{ct}$ ) of the NHCS-SnS<sub>2</sub>/S electrode was 2 and 34  $\Omega$ , respectively, shows no difference to the NHCS/S electrode. After cycled at 0.5 C for 200 cycles, related to the electrolyte infiltration, rearrangement, and activation of sulfur,<sup>[46]</sup> the Nyquist plots of both two electrodes show a distinct decrease of  $R_{ct}$  values (Figure 3i). However, for the NHCS-SnS<sub>2</sub>/S electrode, the value of  $R_{ct}$  (9.6  $\Omega$ ) and the resistance of solid electrolyte interface ( $R_e$ , 6.5  $\Omega$ ) is considerably smaller than that of NHCS/S electrode, indicating the polar SnS<sub>2</sub> could bring about fast charge transfer rate and effectively improve the redox kinetics. What is more, lower Warburg coefficient of NHCS-SnS<sub>2</sub>/S cathode after cycled compared to the NHCS/S cathode indicates the higher ion diffusion rate arising from SnS<sub>2</sub> decorating (Figure 3j). Ex situ SEM images (Figure S14, Supporting Information) further exhibit that almost no agglomeration of Li<sub>2</sub>S<sub>x</sub> could be found on the NHCS-SnS<sub>2</sub>/S electrode. However, the NHCS/S electrode after cycling exhibit expanded massive Li<sub>2</sub>S<sub>x</sub> covering the clusters of hollow spheres as marked by dash line. Which extremely clarified that SnS<sub>2</sub> decoration can not only alleviate LIPSS shutting but also promote the uniform nucleation of Li<sub>2</sub>S thus keep the ion path unblocked. All these factors lead to the outstanding cycling performance.

### 2.3. Catalytic Effect on LIPSS Conversion

To investigate the catalytic effect of SnS<sub>2</sub> modification on LIPSS conversion, NHCS-SnS<sub>2</sub>/S was washed by CS<sub>2</sub> solution to remove element sulfur. The CV test of Li<sub>2</sub>S<sub>6</sub> symmetric cells

was conducted at the scan rate of 10 mV s<sup>-1</sup> between -0.8 and 0.8 V. As shown in Figure 4a, without Li<sub>2</sub>S<sub>6</sub> addition, almost no contribution of capacitive current could be achieved. In the electrolyte with Li<sub>2</sub>S<sub>6</sub> (0.2 M) addition, two oxidation peaks located at 0.17 and 0.56 V represent the oxidation of Li<sub>2</sub>S to Li<sub>2</sub>S<sub>6</sub> and Li<sub>2</sub>S<sub>6</sub> to S and the reduction of S to Li<sub>2</sub>S was revealed through the two reduction peaks at -0.17 and -0.56 V.<sup>[47]</sup> Obviously, NHCS-SnS<sub>2</sub> electrode showed higher current response higher redox charge, and narrower peak separation than NHCS electrode (-0.21 and -0.71 V), indicating the fast kinetic of LIPSS conversion. Apart from accelerating the liquid phase LIPSS conversion, potentiostatic (2.09 V) discharge process<sup>[48]</sup> was conducted to investigate the nucleation of Li<sub>2</sub>S on NHCS and NHCS-SnS<sub>2</sub>. Both of them were coated on the carbon paper substrate as cathodes and a Li<sub>2</sub>S<sub>8</sub> (0.5 M) catholyte was added into the cathode side. As shown in Figure 4b,c, the capacity of Li<sub>2</sub>S precipitations on NHCS-SnS<sub>2</sub> electrode was calculated as 185 mAh g<sup>-1</sup><sub>sulfur</sub>, much higher than that on the NHCS electrode (117 mAh g<sup>-1</sup><sub>sulfur</sub>). The results manifest that the incorporation of SnS<sub>2</sub> can not only facilitate the liquid phase transformation but also reduce the nucleation energy of Li<sub>2</sub>S, which is corresponded to the EIS analysis. To evaluate the LIPSS-adsorption ability, the as prepared NHCS and NHCS-SnS<sub>2</sub> were immersed into the pure Li<sub>2</sub>S<sub>6</sub> solution (2 × 10<sup>-3</sup> M in DOL (1,3-dioxolane)/DME (1,2-dimethoxyethane) = 1/1). After soaked for 12 h, NHCS-SnS<sub>2</sub> discolors the Li<sub>2</sub>S<sub>6</sub> solution visibly, while the color of solution with NHCS addition has not decolorized significantly (Figure S15a, Supporting Information), consistent with the UV-vis spectra results (Figure S15b, Supporting Information). To unveil the mechanic of chemical interaction between SnS<sub>2</sub> and LIPSS, XPS spectra of NHCS-SnS<sub>2</sub> after soaked in Li<sub>2</sub>S<sub>6</sub> solution are shown in Figure 4d-f. In the Sn 3d spectra,

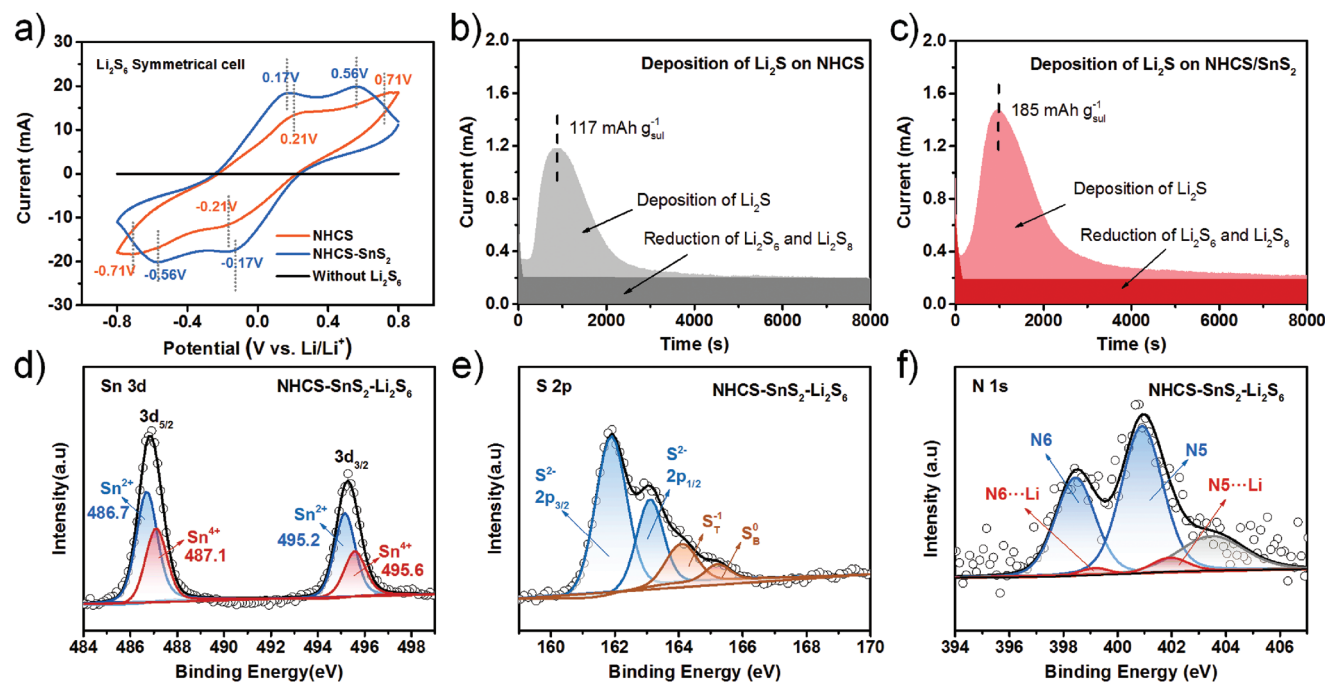


**Figure 4.** a) CV curves of Li<sub>2</sub>S<sub>6</sub> and Li<sub>2</sub>S<sub>6</sub>-free symmetric batteries with identical electrodes. b,c) Potentiostatic discharge curves at 2.09 V of NHCS and NHCS-SnS<sub>2</sub> cathode based on Li<sub>2</sub>S<sub>8</sub> catholyte (0.5 M). d-f) XPS spectra of Sn3d, S2p, and N1s of NHCS-SnS<sub>2</sub> after soaked in Li<sub>2</sub>S<sub>6</sub> solution.

after contact with  $\text{Li}_2\text{S}_6$ , the two newly formed peaks located at 486.7 and 495.15 eV attributed to  $\text{Sn}^{2+} 3d_{5/2}$  and  $\text{Sn}^{2+} 3d_{3/2}$ ,<sup>[49]</sup> which shift toward comparatively lower binding energy than original  $\text{Sn}^{4+}$ , indicating the enhanced electron density, which is ascribed to the Lewis-acid interaction between the Sn atoms and the S atoms in LIPSS species.<sup>[50]</sup> Accordingly, apart from the peaks belonged to  $\text{SnS}_2$  (161.9/163 eV) in the S 2p spectra, two peaks around 164.08 and 165.21 eV assigned to  $\text{S}_T^{-1}$  and  $\text{S}_B^0$  atoms in  $\text{Li}_2\text{S}_6$  also demonstrate a positive shift compared to the value in pure  $\text{Li}_2\text{S}_6$  as reported caused by electrons losing.<sup>[42a,51]</sup> What's more, the N 1s spectra exhibit two peaks at 399.15 and 401.93 eV, suggesting the Lewis-acid interaction between N and the  $\text{Li}^+$  in LIPSS, which were mainly contributed by pyrrolic N (N5) and pyridinic N (N6).<sup>[18]</sup> The residual electron pair in N5 or N6 can provide strong electrostatic interaction with terminal Li atoms in poly sulfides.<sup>[52]</sup> Likewise, the peak indexed to Li–N bond located at 56.55 eV could also be identified in the Li 1s spectra (Figure S16, Supporting Information).<sup>[9a]</sup> XPS tests further demonstrate that the NHCS- $\text{SnS}_2$  hybrid structure could play an outstanding cooperative immobilization effect of LIPSS toward Li–N bond and S–Sn bond.

To go deep into the chemical interaction mechanism between  $\text{SnS}_2$  and LIPSSs deeply, theoretical simulations were employed to figure out the binding energies between  $\text{SnS}_2$  and LIPSSs species through the density functional theory (DFT) method. Here,  $\text{Li}_2\text{S}_4$  was used as the representative of LIPSSs for modeling. Meanwhile, facet (101) and (001) for  $\text{SnS}_2$  were set as the anchor plane for  $\text{Li}_2\text{S}_4$ . As shown in Figure 5a, the binding energies between the (101) plane and the (101) plane of  $\text{SnS}_2$  with  $\text{Li}_2\text{S}_4$  were calculated to be  $-1.10$  and  $-2.15$  eV, respectively. These values endow a moderate LIPSSs chemical anchoring ability of  $\text{SnS}_2$  among the results have been reported.<sup>[15b]</sup> What is more, the chemisorption ability is mainly originated to the chemical binding between the sulfur atoms in  $\text{Li}_2\text{S}_4$  and the Sn in  $\text{SnS}_2$  on the (101) plane meanwhile, the Li– $\text{S}^*$  bonding is calculated to dominate the chemisorption on the (001) plane. Based on the effective capture of LIPSSs,

the diffusion barriers of Li-ion and  $\text{Li}_2\text{S}_4$  on the surface of  $\text{SnS}_2$  were investigated to estimate the acceleration of reduction process of LIPSSs. The minimum energy path for Li-ion diffusion on the (001) and the (101) plane of  $\text{SnS}_2$  were illustrated in Figure S17 in the Supporting Information, and the corresponding diffusions barriers were calculated to be 0.14 and 0.33 eV, respectively, much smaller than the barriers on the bare carbon matrix or graphite as reported.<sup>[12,24]</sup> On the other hand, in Figure 5b, the minimum energy migration path for  $\text{Li}_2\text{S}_4$  on the (001) and (101)  $\text{SnS}_2$  surface was shown, and the migration barriers are 0.12 and 0.79 eV, respectively. All these calculations theoretically confirm that the  $\text{SnS}_2$  can offer stronger chemical adsorption of polysulfides, faster Li-ion and LIPSSs transference than bare carbon matrix. Based on the chemisorption test, nucleation test and EIS results mentioned before, thus further elucidate that the modification of  $\text{SnS}_2$  on NHCS can activate the carbon- $\text{SnS}_2$ -electrolyte triple phase catalytic effect of intermediate products conversion in electrolyte and facilitate the uniform deposition of final  $\text{Li}_2\text{S}$  species on the carbon matrix through a novel capture-diffusion-nucleation mechanism as reported. The probable schematic of the catalytic mechanism is shown in Figure 5c. Long-chain LIPSSs were captured by  $\text{SnS}_2$  first, then gained electrons and  $\text{Li}^+$  on the polar surfaced followed by conversed to short-chain LIPSSs through the lowest migration barrier path. Finally, solid product  $\text{Li}_2\text{S}$  formed uniformly adjacent to the interfaces between  $\text{SnS}_2$  polar sites and carbon matrix.

### 3. Conclusion

NHCS- $\text{SnS}_2$ /S hybrid hollow spheres bring about a conversion route from sulfur to polysulfides and further to  $\text{Li}_2\text{S}$  through the capture-diffusion-nucleation mechanism. The as prepared cathodes delivered higher sulfur utilization and triggers the LIPSSs shuttling more efficiently than the bare NHCS. Even at high sulfur loading, NHCS- $\text{SnS}_2$ /S cathode still achieved remarkable

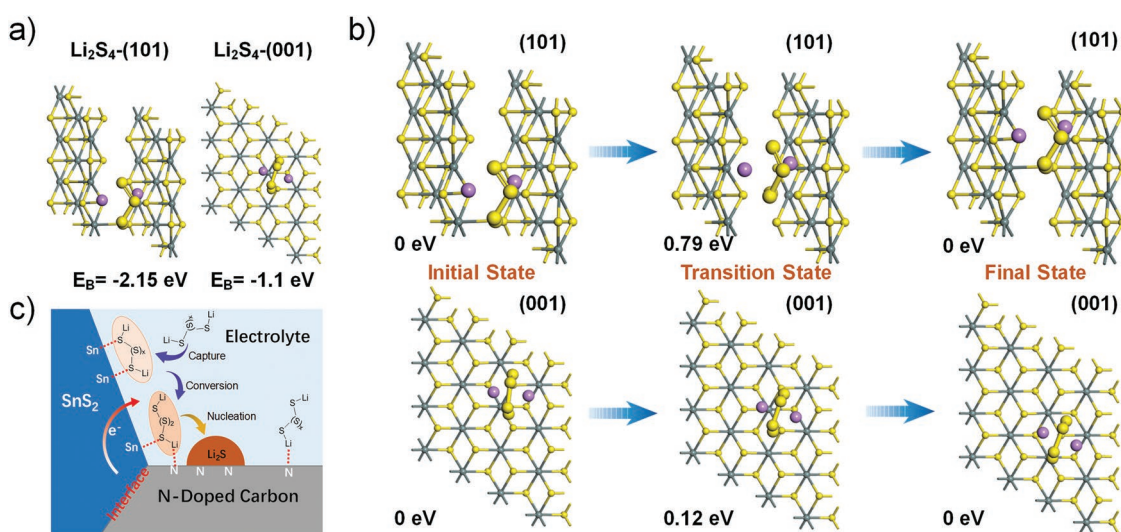


**Figure 5.** a) Theoretical calculation and characteristics of anchoring of  $\text{Li}_2\text{S}_4$  on  $\text{SnS}_2$  (001) and (101) surface. b) Initial, transition, and final state of  $\text{Li}_2\text{S}_4$  on the minimum energy path way on  $\text{SnS}_2$  (101) surface and (001) surface. Yellow, gray, and purple balls represent S, Sn, and Li atoms, respectively. c) The diagram of triple phase interfaces catalytic effect on the carbon shell.



rate performance and high capacity retention. It all arise from such unique hybrid structure integrated the electroconductivity of carbon matrix, ion-conductivity of electrolyte, and the polarity of SnS<sub>2</sub> together, thus further gestated the triple-phase interfaces catalyst effect and bring the advantages of each part materials into full play. The experiments and calculation collectively suggest this hollow carbon shells modified with nitrogen and decorated with SnS<sub>2</sub> are effective host for sulfur cathode for Li–S batteries.

## 4. Experimental Section

**Synthesis of N-Doped Hollow Carbon Spheres (NHCS):** NHCS was prepared by a surfactant-free strategy coupled with a facile hydrothermal method. In a typical method, 70 mL ethanol, 10 mL deionized water, and 3 mL ammonia water (25–28%) were mixed together for 10 min under stirring. Then 3.46 mL TEOS was dropped into the above solution and kept stirring for 15 min. Subsequently, 0.2 g resorcinol and 0.28 mL formaldehyde (37 wt% in H<sub>2</sub>O) were successively added into the white suspension carefully and kept stirring at room temperature for 24 h until the mixture turned dark and then, the reddish-brown precursor was obtained by centrifugation. Later, the precursor was annealed at 350 °C for 2 h and 750 °C for 5 h at the heating rate of 2 °C min<sup>-1</sup> under N<sub>2</sub> protection followed by etching silica with NaOH aqueous solution (2 M, 100 mL for 0.1 g SiO<sub>2</sub>@C) under 60 °C. Finally, the black powder was dispersed in 30 mL ammonia water (25–28 wt%) by sonicated and sealed in a 50 mL Teflon-lined stainless-steel autoclave and reacted at 180 °C for 9 h in succession. The product was washed by water and dried in a vacuum oven at 60 °C.

**Synthesis of NHCS-SnO<sub>2</sub>:** Typically, 120 mg as prepared NHCS were dispersed in 100 mL solution (water /ethanol = 3/1 v/v) by sonicated for 30 min to obtain a black suspension. Meanwhile, 50 mg SnCl<sub>2</sub>·2H<sub>2</sub>O was dissolved in a 100 mL solution containing 99 mL deionized water and 1 mL hydrochloric acid under stirring for 5 min to obtain a transparent solution. Next, the NHCS suspension was added into above solution quickly and kept stirring vigorously at 50 °C for 12 h. After that, the product was collected by centrifugation and washed by water and ethanol for three times. The obtained black powder was dried at 80 °C in a vacuum oven overnight followed by calcined at 500 °C for 3 h under Ar protection.

**Synthesis of NHCS-SnS<sub>2</sub>/S Composite:** The as synthesized NHCS-SnO<sub>2</sub> precursor was grinded with sulfur powder with a weight ratio of 1/3 in an agate mortar for 30 min. Then, the mixed powder was sealed in a vacuum amputated glass bottle. Then, it was heated in a tubular furnace at 155 °C for 12 h and 300 °C for 5 h. NHCS/S was prepared by same process. NHCS-SnS<sub>2</sub> composite for XRD, adsorption test, symmetric cells, and Li<sub>2</sub>S nucleation test was prepared by washing NHCS-SnS<sub>2</sub>/S composite mentioned above by using CS<sub>2</sub> solution.

**Materials Characterization:** The crystalline phases of samples were tested by XRD (Bruker D8 Advance), using Cu K<sub>α</sub> radiation (λ = 0.15418 nm). The morphologies and particle size of samples were characterized by using SEM (ZEISS SUPRA55). HRTEM (Field Electron and Ion Co. Tecnai G2 F30) combined with EDS was employed to characterize the lattice fringe and the elements distribution of the samples. The element and electronic environment of the samples were investigated by XPS (PHI 5000 V Versa Probe II). The contents of sulfur and carbon in the composite were analyzed by thermal gravimetric analysis measured under N<sub>2</sub> and air flow respectively at a heating rate of 10 °C min<sup>-1</sup>. Raman spectra were collected by employing Raman tester (HORIBA, LabRam HR800) and using 532 nm laser excitation in the range of 200–2000 cm<sup>-1</sup>. The data of specific surface area, pore volume, and distribution of pore size were determined by gas sorption analyzer (Micromeritics-ASAP 2020). The absorption spectra of Li<sub>2</sub>S<sub>6</sub> in DOL/DME (1/1 v/v) solution were carried out by ultraviolet-visible (UV-vis, UV-2550 spectrophotometer, Shimadzu), and the blank solution was measured as reference.

**Electrochemical Measurements:** Li–S batteries cathodes were prepared by mixing NHCS-SnS<sub>2</sub>/S or NHCS/S, Super P, carboxymethylcellulose sodium, and styrene butadiene rubber (1/1 in weight) in a weight ratio of 7:2:1 and stirred for 4 h with the aid of amount of deionized water to obtain a homogenous slurry. Then, the slurry was coated on the Al foil by using a doctor blade. After dried at 60 °C overnight in a vacuum oven, the electrodes were punched into 10 mm disks with a low sulfur loading of 0.8–1.0 mg cm<sup>-2</sup> and a high area sulfur loading of 3.0–3.2 mg cm<sup>-2</sup>. 2032 coin cells were assembled in a glovebox under Ar atmosphere protection. The electrolyte was 1 M lithium bis(trifluoromethanesulfonyl) imide (LITFSI) in a mixed solution of DOL/DME (1/1 v/v) with 2 wt% LiNO<sub>3</sub> and the ratio of electrolyte to sulfur was measured about 20 μL per 1 mg of sulfur. The galvanostatic discharge and charge tests were carried out by LAND CT2100A (5 V, 10 mA, Wuhan LANHE) with a potential range of 1.7–2.8 V versus Li/Li<sup>+</sup> and the value of specific capacity was calculated based on the weight of sulfur. CV curves, EIS results were collected by electrochemical workstation (Gamry Interface 1000, Germany). Respectively, CV curves were performed from 1.5–3 V at a scanning rate of 0.1 mV s<sup>-1</sup> and the frequency of EIS patterns were measured from 100 kHz to 0.01 Hz, the Ac amplitude of EIS measurements is 5 mV.

**Li<sub>2</sub>S Nucleation Test:** The NHCS or NHCS-SnS<sub>2</sub> was composited with poly(vinylidene fluoride) at the ratio of 8/1 and mixed by N-methyl-2-pyrrolidone followed by coated on a carbon paper with the mass loading around 1.5 mg cm<sup>-2</sup>. The electrode was punched into disks with diameter around 10 mm. Li-foil was served as anode. And the 20 μL catholyte consisting of 1M LITFSI in DOL/DME = 1/1 v/v with Li<sub>2</sub>S<sub>8</sub> addition (0.5 M) was added to the cathode side. The cell was first discharged to 2.10 V under the current of 0.134 mA galvanostatically and then kept at 2.09 V potentiostatically for Li<sub>2</sub>S to nucleate and grow. The curve from 0 to 8000 s was calculated to measure the capacity of Li<sub>2</sub>S nucleation by Faraday's law.

**Computational Method:** All the spin polarized geometric optimizations, single-point energies, and electronic structures calculations were performed with the Vienna ab initio simulation package code,<sup>[53]</sup> using the general gradient approximation-Perdew-Burke-Ernzerhof functional<sup>[54]</sup> of DFT and the projector augmented wave method<sup>[55]</sup> to account for the core–valence interactions. For all the calculations, 500 eV was chosen as the cutoff energy of the plane-wave basis to ensure the precision of calculations. The (001) and (101) surface of SnS<sub>2</sub> were used to represent the catalytic interface, as they were abundantly exposed in experimental situations. During the structure optimizations, the atoms in the bottom three layers were fixed, while the atoms in the top layers were fully relaxed. At least 20 Å vacuum layer was applied in z-direction of the slab models to prevent the vertical interactions between slabs. A 3 × 3 × 1 Monkhorst–Pack grid<sup>[56]</sup> was used to carry out the surface calculations on all the models. The convergence thresholds for structural optimization were set at 0.02 eV Å<sup>-1</sup> in force. The convergence criterion for energy is 10<sup>-5</sup> eV. The van der Waals (vdW) dispersion by employing the D3 method of Grimme was considered for all the calculations.<sup>[57]</sup> The climbing image nudged elastic band<sup>[58]</sup> was applied for computing the diffusion barriers, which can obtain the minimum energy path between the optimized initial and final positions.

The binding energy between the Li<sub>2</sub>S<sub>4</sub> and the substrate is defined by Equation (1)

$$E_{\text{binding}} = E_{\text{Li}_2\text{S}_4@_{\text{sub}}} - E_{\text{sub}} + E_{\text{Li}_2\text{S}_4} \quad (1)$$

where  $E_{\text{Li}_2\text{S}_4@_{\text{sub}}}$  is the total energy of substrate with an adsorbed Li<sub>2</sub>S<sub>4</sub> cluster,  $E_{\text{sub}}$  is the total energy of substrates, and  $E_{\text{Li}_2\text{S}_4}$  is the total energy of single Li<sub>2</sub>S<sub>4</sub> cluster in vacuum.

## Supporting Information

Supporting Information is available from the Wiley Online Library or from the author.



## Acknowledgements

This work was financially supported by Shenzhen Basic Research Project Funds (JCYJ20170817161127616).

## Conflict of Interest

The authors declare no conflict of interest.

## Keywords

catalytic effect, fast kinetic, hybrid hollow spheres, Li–sulfur batteries, triple phase interface

Received: August 14, 2019

Revised: October 4, 2019

Published online: November 22, 2019

- [1] Y. Yang, G. Zheng, Y. Cui, *Chem. Soc. Rev.* **2013**, 42, 3018.
- [2] Z. W. Seh, Y. Sun, Q. Zhang, Y. Cui, *Chem. Soc. Rev.* **2016**, 45, 5605.
- [3] Z.-W. Zhang, H.-J. Peng, M. Zhao, J.-Q. Huang, *Adv. Funct. Mater.* **2018**, 28, 1707536.
- [4] X. Ji, K. T. Lee, L. F. Nazar, *Nat. Mater.* **2009**, 8, 500.
- [5] L. Sun, M. Li, Y. Jiang, W. Kong, K. Jiang, J. Wang, S. Fan, *Nano Lett.* **2014**, 14, 4044.
- [6] L. Ji, M. Rao, H. Zheng, L. Zhang, Y. Li, W. Duan, J. Guo, E. J. Cairns, Y. Zhang, *J. Am. Chem. Soc.* **2011**, 133, 18522.
- [7] N. Jayaprakash, J. Shen, S. S. Moganty, A. Corona, L. A. Archer, *Angew. Chem., Int. Ed.* **2011**, 50, 5904.
- [8] G. Zheng, Q. Zhang, J. J. Cha, Y. Yang, W. Li, Z. W. Seh, Y. Cui, *Nano Lett.* **2013**, 13, 1265.
- [9] a) Q. Pang, J. Tang, H. Huang, X. Liang, C. Hart, K. C. Tam, L. F. Nazar, *Adv. Mater.* **2015**, 27, 6021; b) Y. Liu, Y. Yan, K. Li, Y. Yu, Q. Wang, M. Liu, *Chem. Commun.* **2019**, 55, 1084.
- [10] X. Liu, J. Q. Huang, Q. Zhang, L. Mai, *Adv. Mater.* **2017**, 29, 161759.
- [11] Z. Wei Seh, W. Li, J. J. Cha, G. Zheng, Y. Yang, M. T. McDowell, P. C. Hsu, Y. Cui, *Nat. Commun.* **2013**, 4, 1331.
- [12] G. Zhou, H. Tian, Y. Jin, X. Tao, B. Liu, R. Zhang, Z. W. Seh, D. Zhuo, Y. Liu, J. Sun, *Proc. Natl. Acad. Sci. U. S. A.* **2017**, 114, 840.
- [13] T. Zhou, Y. Zhao, G. Zhou, W. Lv, P. Sun, F. Kang, B. Li, Q. H. Yang, *Nano Energy* **2017**, 39, 291.
- [14] W. G. Lim, C. Jo, A. Cho, J. Hwang, S. Kim, J. W. Han, J. Lee, *Adv. Mater.* **2019**, 31, 1806547.
- [15] a) C. Li, Z. Xi, D. Guo, X. Chen, L. Yin, *Small* **2018**, 14, 1701986; b) Q. Zhang, Y. Wang, Z. W. Seh, Z. Fu, R. Zhang, Y. Cui, *Nano Lett.* **2015**, 15, 3780.
- [16] Y. Tao, Y. Wei, Y. Liu, J. Wang, W. Qiao, L. Ling, D. Long, *Energy Environ. Sci.* **2016**, 9, 3230.
- [17] a) X. Tao, J. Wang, C. Liu, H. Wang, H. Yao, G. Zheng, Z. W. Seh, Q. Cai, W. Li, G. Zhou, C. Zu, Y. Cui, *Nat. Commun.* **2016**, 7, 11203; b) H. J. Peng, G. Zhang, X. Chen, Z. W. Zhang, W. T. Xu, J. Q. Huang, Q. Zhang, *Angew. Chem., Int. Ed.* **2016**, 55, 12990; c) H. Yuan, H.-J. Peng, B.-Q. Li, J. Xie, L. Kong, M. Zhao, X. Chen, J.-Q. Huang, Q. Zhang, *Adv. Energy Mater.* **2019**, 9, 1802768.
- [18] H. J. Peng, Z. W. Zhang, J. Q. Huang, G. Zhang, J. Xie, W. T. Xu, J. L. Shi, X. Chen, X. B. Cheng, Q. Zhang, *Adv. Mater.* **2016**, 28, 9551.
- [19] T. Zhou, W. Lv, J. Li, G. Zhou, Y. Zhao, S. Fan, B. Liu, B. Li, F. Kang, Q.-H. Yang, *Energy Environ. Sci.* **2017**, 10, 1694.
- [20] Y. Song, W. Zhao, L. Kong, L. Zhang, X. Zhu, Y. Shao, F. Ding, Q. Zhang, J. Sun, Z. Liu, *Energy Environ. Sci.* **2018**, 11, 2620.
- [21] C. Dai, J.-M. Lim, M. Wang, L. Hu, Y. Chen, Z. Chen, H. Chen, S.-J. Bao, B. Shen, Y. Li, G. Henkelman, M. Xu, *Adv. Funct. Mater.* **2018**, 28, 1704443.
- [22] L. Luo, S.-H. Chung, A. Manthiram, *Adv. Energy Mater.* **2018**, 8, 1801014.
- [23] S. S. Zhang, D. T. Tran, *J. Mater. Chem. A* **2016**, 4, 4371.
- [24] J. Xu, W. Zhang, H. Fan, F. Cheng, D. Su, G. Wang, *Nano Energy* **2018**, 51, 73.
- [25] Z. Cheng, Z. Xiao, H. Pan, S. Wang, R. Wang, *Adv. Energy Mater.* **2018**, 8, 1702337.
- [26] a) L. Luo, S.-H. Chung, A. Manthiram, *J. Mater. Chem. A* **2018**, 6, 7659; b) X. Li, L. Chu, Y. Wang, L. Pan, *Mater. Sci. Eng., B* **2016**, 205, 46.
- [27] Z. Yuan, H.-J. Peng, T.-Z. Hou, J.-Q. Huang, C.-M. Chen, D.-W. Wang, X.-B. Cheng, F. Wei, Q. Zhang, *Nano Lett.* **2016**, 16, 519.
- [28] T. Lei, W. Chen, J. Huang, C. Yan, H. Sun, C. Wang, W. Zhang, Y. Li, J. Xiong, *Adv. Energy Mater.* **2017**, 7, 1601843.
- [29] a) X. Chen, H.-J. Peng, R. Zhang, T.-Z. Hou, J.-Q. Huang, B. Li, Q. Zhang, *ACS Energy Lett.* **2017**, 2, 795; b) Q. Pang, X. Liang, C. Y. Kwok, L. F. Nazar, *Nat. Energy* **2016**, 1, 16132.
- [30] a) Z. Li, J. Zhang, B. Guan, D. Wang, L. M. Liu, X. W. Lou, *Nat. Commun.* **2016**, 7, 13065; b) C. Ye, L. Zhang, C. Guo, D. Li, A. Vasileff, H. Wang, S.-Z. Qiao, *Adv. Funct. Mater.* **2017**, 27, 1702524; c) J. He, L. Luo, Y. Chen, A. Manthiram, *Adv. Mater.* **2017**, 29, 1702707.
- [31] Z.-A. Qiao, B. Guo, A. J. Binder, J. Chen, G. M. Veith, S. Dai, *Nano Lett.* **2013**, 13, 207.
- [32] H. Zhang, O. Noonan, X. Huang, Y. Yang, C. Xu, L. Zhou, C. Yu, *ACS Nano* **2016**, 10, 4579.
- [33] L. Liu, H. Zhao, L. Shi, M. Lan, H. Zhang, C. Yu, *Electrochim. Acta* **2017**, 227, 69.
- [34] Q. Shao, J. Tang, Y. Sun, J. Li, K. Zhang, J. Yuan, D. M. Zhu, L. C. Qin, *Nanoscale* **2017**, 9, 4439.
- [35] a) Y. Liu, Y. Yang, X. Wang, Y. Dong, Y. Tang, Z. Yu, Z. Zhao, J. Qiu, *ACS Appl. Mater. Interfaces* **2017**, 9, 15484; b) L. Fan, X. Li, X. Song, N. Hu, D. Xiong, A. Koo, X. Sun, *ACS Appl. Mater. Interfaces* **2018**, 10, 2637.
- [36] Z. Xu, T. Wang, L. Kong, K. Yao, H. Fu, K. Li, L. Cao, J. Huang, Q. Zhang, *Part. Part. Syst. Charact.* **2017**, 34, 1600223.
- [37] S. Chen, X. Huang, B. Sun, J. Zhang, H. Liu, G. Wang, *J. Mater. Chem. A* **2014**, 2, 16199.
- [38] a) L. Lin, H. Xing, R. Shu, L. Wang, X. Ji, D. Tan, Y. Gan, *RSC Adv.* **2015**, 5, 94539; b) S. Huang, M. Wang, P. Jia, B. Wang, J. Zhang, Y. Zhao, *Energy Storage Mater.* **2019**, 20, 225.
- [39] a) R. Pongilat, K. Nallathamby, *ACS Appl. Mater. Interfaces* **2018**, 10, 38853; b) R. Yang, H. Du, Z. Lin, L. Yang, H. Zhu, H. Zhang, Z. Tang, X. Gui, *Carbon* **2019**, 141, 258; c) A. Chen, W. Liu, H. Hu, T. Chen, B. Ling, K. Liu, *J. Mater. Chem. A* **2018**, 6, 20083.
- [40] X. Liang, C. Hart, Q. Pang, A. Garsuch, T. Weiss, L. F. Nazar, *Nat. Commun.* **2015**, 6, 5682.
- [41] a) Q. Sun, B. Xi, J.-Y. Li, H. Mao, X. Ma, J. Liang, J. Feng, S. Xiong, *Adv. Energy Mater.* **2018**, 8, 1800595; b) G. Zhou, Y. Zhao, A. Manthiram, *Adv. Energy Mater.* **2015**, 5, 1402263.
- [42] a) Z. Xing, G. Li, S. Sy, Z. Chen, *Nano Energy* **2018**, 54, 1; b) Y. Jiang, Y. Guo, W. Lu, Z. Feng, B. Xi, S. Kai, J. Zhang, J. Feng, S. Xiong, *ACS Appl. Mater. Interfaces* **2017**, 9, 27697.
- [43] C. Zu, A. Manthiram, *Adv. Energy Mater.* **2013**, 3, 1008.
- [44] S. Choudhury, P. Srimuk, K. Raju, A. Tolosa, S. Fleischmann, M. Zeiger, K. I. Ozoemena, L. Borchardt, V. Presser, *Sustainable Energy Fuels* **2018**, 2, 133.
- [45] P. Ji, B. Shang, Q. Peng, X. Hu, J. Wei, *J. Power Sources* **2018**, 400, 572.

- [46] a) R. Wang, K. Wang, S. Gao, M. Jiang, M. Zhou, S. Cheng, K. Jiang, *Nanoscale* **2017**, *9*, 14881; b) Q. Liu, J. Zhang, S. A. He, R. Zou, C. Xu, Z. Cui, X. Huang, G. Guan, W. Zhang, K. Xu, J. Hu, *Small* **2018**, *14*, 1703816.
- [47] a) H. Lin, L. Yang, X. Jiang, G. Li, T. Zhang, Q. Yao, G. W. Zheng, J. Y. Lee, *Energy Environ. Sci.* **2017**, *10*, 1476; b) S. Huang, Y. V. Lim, X. Zhang, Y. Wang, Y. Zheng, D. Kong, M. Ding, S. A. Yang, H. Y. Yang, *Nano Energy* **2018**, *51*, 340.
- [48] a) F. Y. Fan, W. C. Carter, Y. M. Chiang, *Adv. Mater.* **2015**, *27*, 5203; b) Z. L. Xu, S. Lin, N. Onofrio, L. Zhou, F. Shi, W. Lu, K. Kang, Q. Zhang, S. P. Lau, *Nat. Commun.* **2018**, *9*, 4164.
- [49] D. Chao, C. Zhu, P. Yang, X. Xia, J. Liu, J. Wang, X. Fan, S. V. Savilov, J. Lin, H. J. Fan, *Nat. Commun.* **2016**, *7*, 12122.
- [50] a) Q. Pang, D. Kundu, M. Cuisinier, L. F. Nazar, *Nat. Commun.* **2014**, *5*, 4759; b) X. Liang, C. Y. Kwok, F. Lodi-Marzano, Q. Pang, M. Cuisinier, H. Huang, C. J. Hart, D. Houtarde, K. Kaup, H. Sommer, T. Brezesinski, J. Janek, L. F. Nazar, *Adv. Energy Mater.* **2016**, *6*, 1501636.
- [51] Y. Wang, R. Zhang, Y.-c. Pang, X. Chen, J. Lang, J. Xu, C. Xiao, H. Li, K. Xi, S. Ding, *Energy Storage Mater.* **2019**, *16*, 228.
- [52] X. Li, Y. Chen, H. Huang, Y.-W. Mai, L. Zhou, *Energy Storage Mater.* **2016**, *5*, 58.
- [53] a) G. Kresse, J. Furthmuller, *Comput. Mater. Sci.* **1996**, *6*, 15; b) G. Kresse, J. Hafner, *Phys. Rev. B* **1994**, *49*, 14251.
- [54] J. P. Perdew, K. Burke, M. Ernzerhof, *Phys. Rev. Lett.* **1996**, *77*, 3865.
- [55] P. E. Blöchl, *Phys. Rev. B* **1994**, *50*, 17953.
- [56] D. J. Chadi, *Phys. Rev. B* **1977**, *16*, 1746.
- [57] S. Grimme, J. Antony, S. Ehrlich, H. Krieg, *J. Chem. Phys.* **2010**, *132*, 154104.
- [58] G. Henkelman, B. P. Uberuaga, H. Jónsson, *J. Chem. Phys.* **2000**, *113*, 9901.